Remote Sensing of Environment 221 (2019) 650–664

Contents lists available at ScienceDirect

Remote Sensing of Environment

journal homepage: www.elsevier.com/locate/rse

Cloud mask-related differential linear adjustment model for MODIS infrared water vapor product

Liang Chang[a,b,c,d,e,*], Ruya Xiao[f], Abhnil Amtesh Prasad[g], Guoping Gao[h], Guiping Feng[a,b,c,d,e], Yu Zhang[a,b,c,d,e]

[a] College of Marine Sciences, Shanghai Ocean University, Shanghai, China
[b] The Key Laboratory of Sustainable Exploitation of Oceanic Fisheries Resources, Ministry of Education, Shanghai Ocean University, Shanghai, China
[c] Engineering Research Center on Estuarine and Oceanographic Mapping, Shanghai Municipal Ocean Bureau, Shanghai, China
[d] National Engineering Research Centre for Oceanic Fisheries, Shanghai Ocean University, Shanghai, China
[e] Key Laboratory of Oceanic Fisheries Exploration, Ministry of Agriculture, Shanghai Municipal Ocean Bureau, Shanghai, China
[f] School of Earth Sciences and Engineering, Hohai University, Nanjing, China
[g] Climate Change Research Centre, University of New South Wales, Sydney, New South Wales, Australia
[h] College of Ocean Science and Engineering, Shanghai Maritime University, Shanghai, China

A R T I C L E I N F O

Keywords:
MODIS
Water vapor
Infrared
Cloud mask
Adjustment model

A B S T R A C T

Water vapor is the primary greenhouse gas of the Earth-atmosphere system and plays a vital role in understanding climate change, if correctly measured from satellites. The Moderate Resolution Imaging Spectroradiometer (MODIS) can monitor water vapor retrievals at near-infrared (nIR) bands in the daytime as well as at infrared (IR) bands in both daytime and night time. However, the accuracy of IR retrievals under confident clear conditions (> 99% probability) is much poorer than that of nIR retrievals. Additionally, IR retrievals under unconfident clear conditions (> 95%, > 66% and ≤66% probabilities) are usually discarded because the possible presence of clouds would further reduce their accuracy. In this study, we develop a cloud mask-related differential linear adjustment model (CDLAM) to adjust IR retrievals under all confident clear conditions. The CDLAM-adjusted IR retrievals are evaluated with the linear least square (LS) adjusted nIR retrievals under confident clear condition and Global Positioning System (GPS) observations under different probabilities of clear conditions. Both case studies in the USA and global (65° S∼65° N) evaluation reveal that the CDLAM can significantly reduce uncertainties in IR retrievals at all clear-sky confidence levels. Moreover, the accuracy of the CDLAM-adjusted IR retrievals under unconfident clear conditions is much better than IR retrievals without adjustment under confident clear conditions, highlighting the effectiveness of the CDLAM in enhancing the accuracy of IR retrievals at all clear-sky confidence levels as well as the data availability improvement of IR retrievals after adjustment with the CDLAM (14% during the analyzed time periods). The most likely reason for the efficiency of the CDLAM may be that the deviation of the differential water vapor information derived by the differential process is significantly shrunken after the linear regression analysis in the presented model. Therefore, the CDLAM is a promising tool for effectively adjusting IR retrievals under all probabilities of clear conditions and can improve our knowledge of the water vapor distribution and variation.

1. Introduction

Water vapor is the most abundant greenhouse gas and exerts significant positive feedbacks for climate warming (Held and Soden, 2000). It has been reported from both climate models and satellite observations that the total amount of atmospheric water vapor could rise at a rate of 7% per Kelvin of surface warming (Wentz et al., 2007). Furthermore, the spatial and temporal phase variability of water vapor is responsible for the vertical stability of the atmosphere, the evolution of the weather and the energy balance of the global climate system (Chahine, 1992). Therefore, accurate measurements of the variability and change of water vapor at global and regional scales are fundamental and critical to our understanding of the climate system.

Radiosonde measurements have been used to estimate the water vapor since the late 1940s. However, they are of little use for long-term climate monitoring, due to the changes in instrumentation and the

* Corresponding author at: College of Marine Sciences, Shanghai Ocean University, Shanghai, China.
E-mail address: chlbwinds@hotmail.com (L. Chang).

https://doi.org/10.1016/j.rse.2018.12.005
Received 12 March 2018; Received in revised form 6 October 2018; Accepted 3 December 2018
Available online 12 December 2018

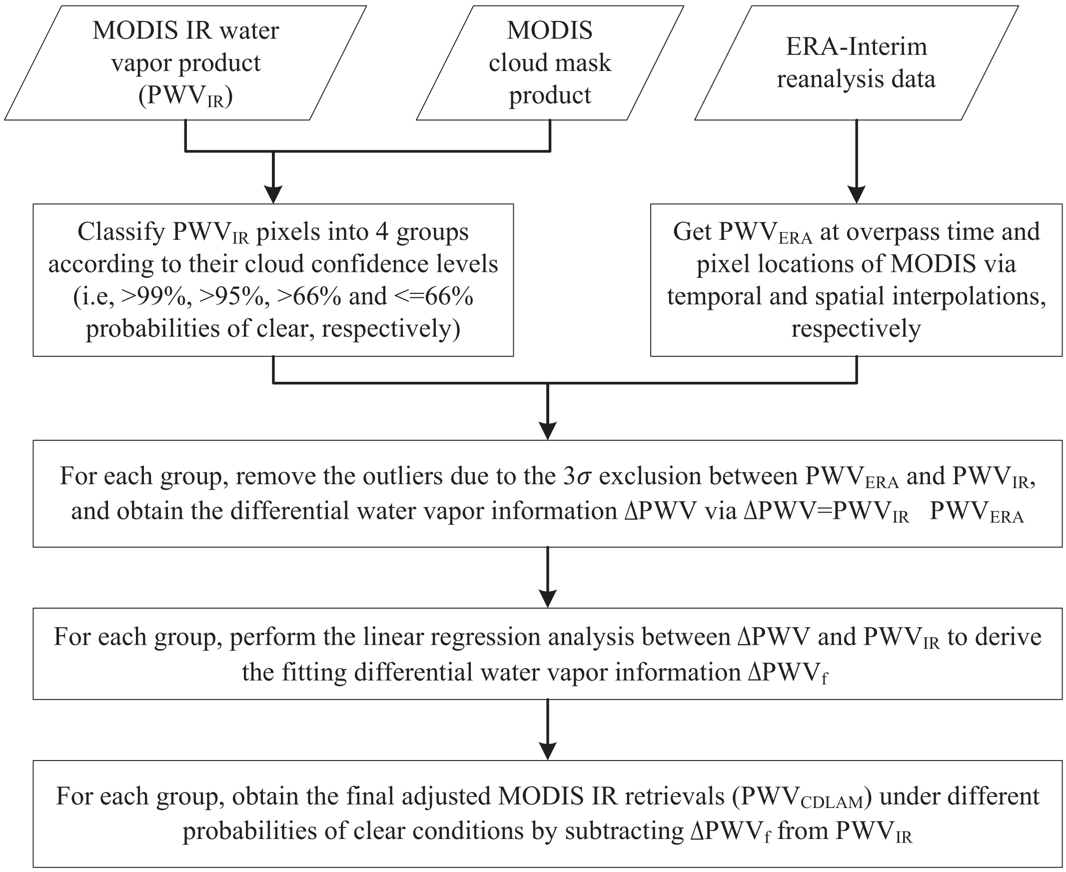

Fig. 1. Flowchart of the cloud mask-related differential linear adjustment model (CDLAM).

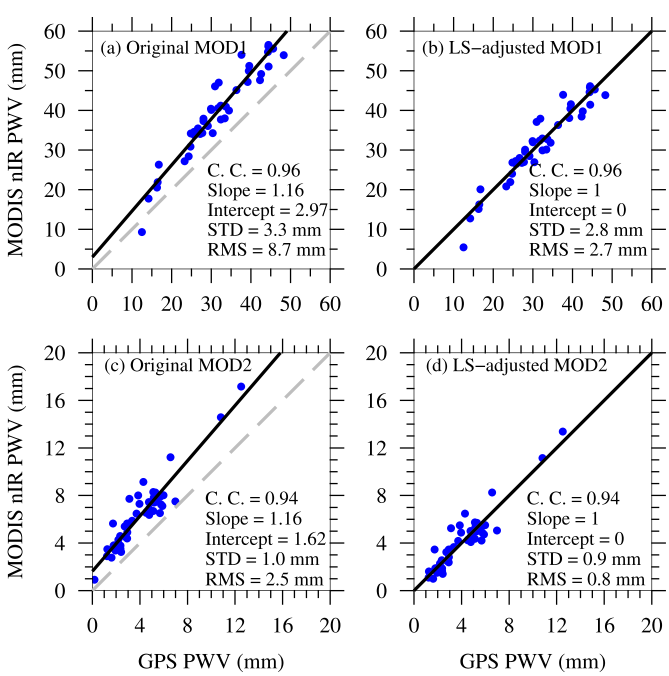

Fig. 2. Scatterplots of the original PWV_{nIR} and PWV_{GPS} in MOD1 (a) and MOD2 (c), as well as the adjusted PWV_{nIR} and PWV_{GPS} in MOD1 (b) and MOD2 (d) under confident clear conditions, respectively. Dashed gray lines: zero-bias lines. Solid black lines: linear regression results.

discontinuities in the resulting data set (McCarthy et al., 2009; Ross and Elliott, 2001). Radiosonde measurements are also fairly sparse over the oceans and the Southern Hemisphere (Li et al., 2003). In contrary, Global Positioning Systems (GPS) can continuously measure precipitable water vapor (PWV) at high temporal resolution in all weather conditions (e.g., Bevis et al., 1994; Yu et al., 2018). Recently, ship-borne GPS observations have been used to measure the PWV over the ocean with the state-of-the-art GPS precise point positioning (PPP) technique (Fan et al., 2016). However, due to the rare and short ship deployments, the GPS observations of PWV are still mainly over land.

Unlike above-ground-based techniques that can only provide point measurements, space-borne monitoring offers a unique opportunity to evaluate the spatial and temporal variability of water vapor on a large or even global scale. Sensors operating in the near-infrared (nIR) bands, such as the Medium Range Resolution Imager Spectrometer (MERIS) (Li et al., 2006; Li et al., 2012) and the Moderate Resolution Imaging Spectroradiometer (MODIS) (Kaufman and Gao, 1992; Li, 2004; Li et al., 2005), can monitor water vapor over both land and ocean in the daytime, but they tend to be affected by the presence of clouds. The atmospheric water vapor amount at infrared (IR) frequencies is also available from instruments such as the Television Infrared Observation Satellite Program (TIROS) Operational Vertical Sounder (TOVS) (Smith et al., 1979), the Advanced TIROS Operational Vertical Sounder (ATOVS) (Li et al., 2000), the Infrared Atmospheric Sounding Interferometer (IASI), the Atmospheric Infrared Sounder (AIRS), the Cross-track Infrared Sounder (CrIS) (Menzel et al., 2018), the MODIS (King et al., 1992) and the Advanced Baseline Imager (ABI) on the Geostationary Operational Environmental Satellites R-series (GOES-R) (Schmit et al., 2005). The IR retrievals can be obtained during both the daytime and night time, are also sensitive to clouds and have poorer accuracy and lower spatial resolution than nIR retrievals.

In order to exclude the possibility of cloud contamination in MODIS

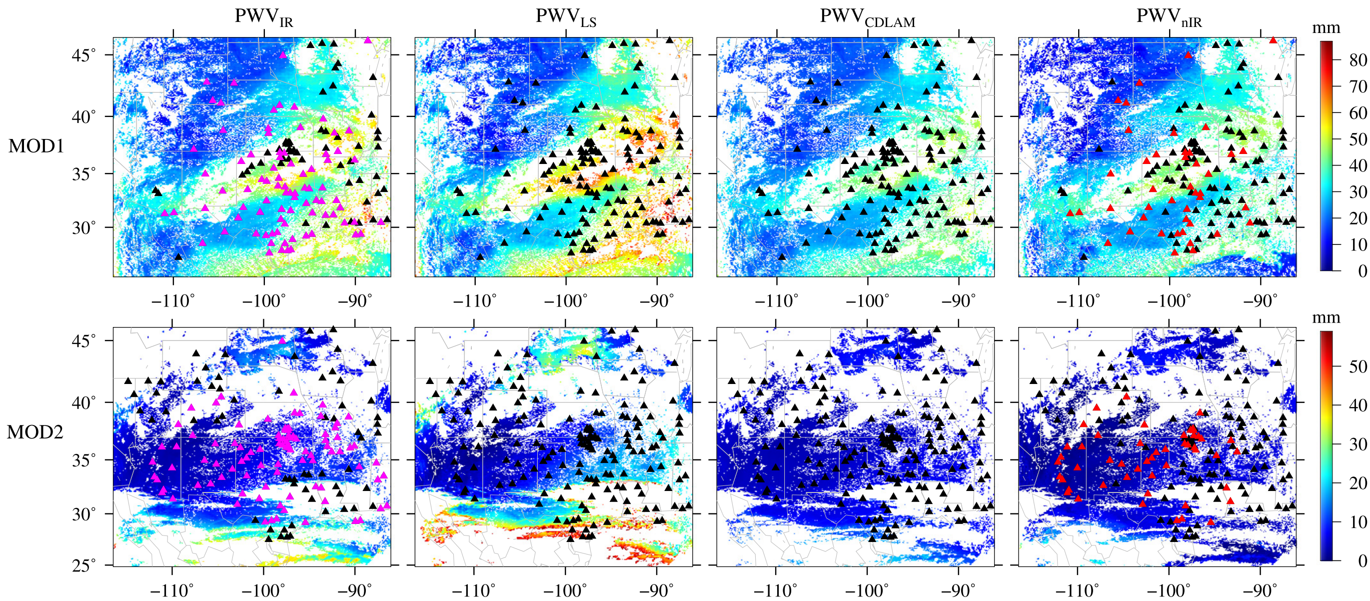

Fig. 3. Water vapor distributions from PWV_{IR}, PWV_{LS}, PWV_{CDLAM} and the adjusted PWV_{nIR}, under confident clear conditions in MOD1 (top row) and MOD2 (bottom row), respectively. Solid black triangles, solid magenta triangles and solid red triangles all denote the locations of GPS sites, while the red ones represent GPS sites used during the linear LS regression analysis in Fig. 2, and the magenta ones are GPS sites used for validation in Fig. 4. (For interpretation of the references to colour in this figure legend, the reader is referred to the web version of this article.)

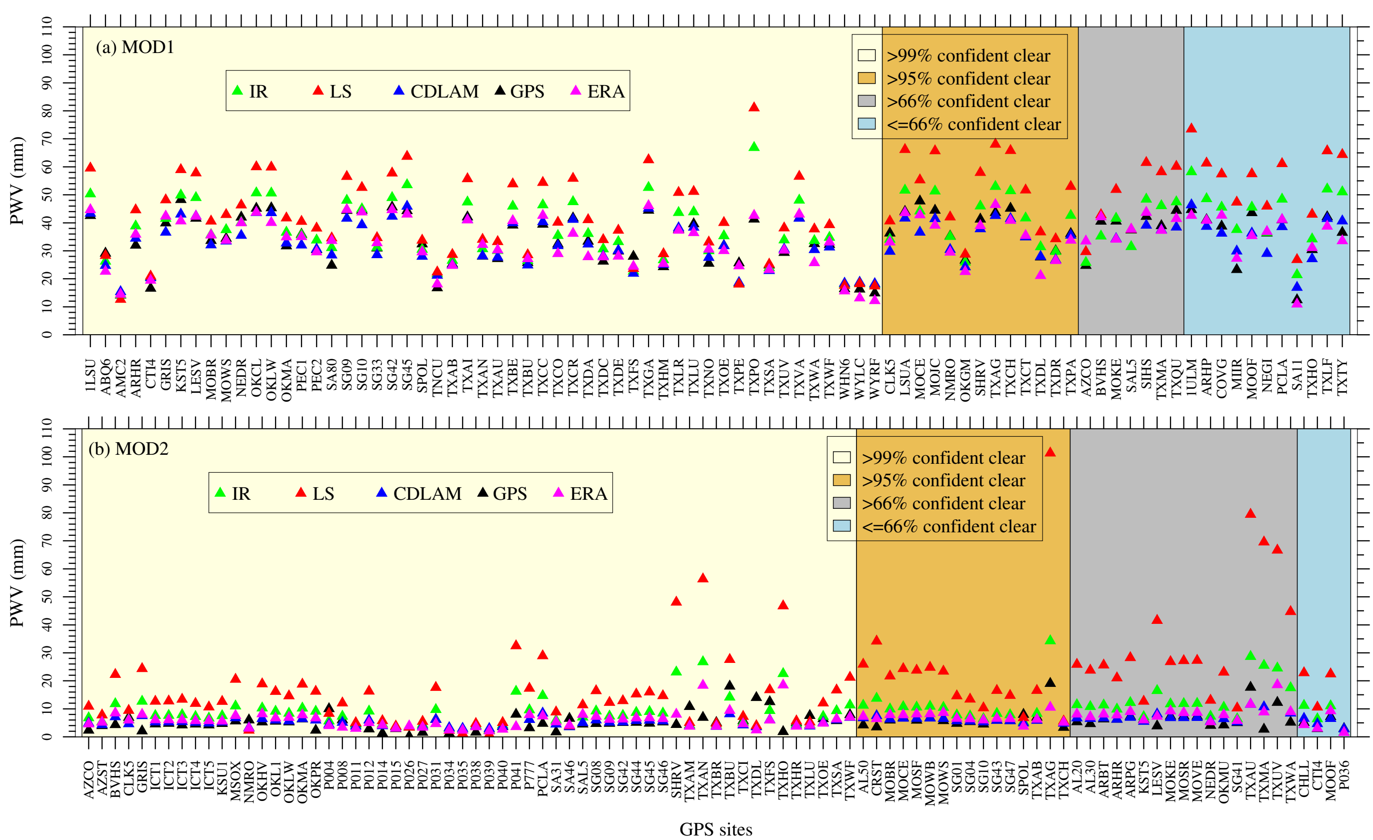

Fig. 4. Comparison of PWV values among PWV_{IR} (green triangles), PWV_{LS} (red triangles), PWV_{CDLAM} (blue triangles), PWV_{ERA} (magenta triangles) and PWV_{GPS} (black triangles) under > 99% (light yellow background), > 95% (gold background), > 66% (gray background) and ≤ 66% (light blue background) probabilities of clear conditions in (a) MOD1 and (b) MOD2, respectively. (For interpretation of the references to colour in this figure legend, the reader is referred to the web version of this article.)

Table 1
The RMS difference of PWV_{IR}, PWV_{LS}, PWV_{CDLAM} and PWV_{ERA} against PWV_{GPS} at different clear-sky confidence levels in MOD1 and MOD2. (Unit: mm).

MODIS image	PWV	Clear-sky confidence level			
		> 99%	> 95%	> 66%	≤66%
MOD1	PWV_{IR}	5.6	5.3	4.8	9.3
	PWV_{LS}	11.1	15.3	12.8	20.3
	PWV_{CDLAM}	2.7	4.4	4.6	4.5
	PWV_{ERA}	3.2	4.0	4.4	3.4
MOD2	PWV_{IR}	6.2	5.7	8.9	4.1
	PWV_{LS}	14.2	25.2	32.3	12.5
	PWV_{CDLAM}	3.1	1.6	3.0	1.2
	PWV_{ERA}	4.3	3.0	3.3	1.3

scenes, generally, only IR retrievals under confident clear conditions (i.e., > 99% probability of clear) were obtained for further applications in previous studies (e.g., Seemann et al., 2003; Liu et al., 2015; Steinke et al., 2015). Moreover, a differential linear calibration model (DLCM) was presented in Chang et al. (2015) to obtain the MODIS PWV information at IR frequencies under confident clear conditions, with better accuracy. Nevertheless, considering that IR retrievals under unconfident clear conditions (i.e., > 95%, > 66% and ≤ 66% probabilities of clear) are also widespread in MODIS IR retrievals, the exploitation of IR retrievals under confident clear conditions only may lose the details of MODIS IR water vapor distribution. In this study, we further develop a cloud mask-related differential linear adjustment model (CDLAM) to derive the improved MODIS IR water vapor retrievals under different probabilities of clear conditions. In section 2, we describe the sources of the data and the methodology. Section 3 carries out two experiments to test the performance of the CDLAM in MODIS IR PWV adjustment for both moist and dry cases in the United States of America (USA). In section 4, global (65° S∼65° N) performance of the CDLAM is evaluated during four different time periods in 2015 via comparison with the adjusted MODIS nIR retrievals as well as the available GPS measurements, respectively. Section 5 discusses the advantages of the CDLAM and the possible reasons for the effectiveness of the CDLAM. Finally, conclusions are drawn in section 6.

2. Data and methodology

2.1. Data

In this paper, the Aqua MODIS Collection 6 Level-1 geolocation (MYD03_L1), Level-2 water vapor (MYD05_L2) and cloud (MYD06_L2) products are used and acquired from the Level-1 and Atmosphere Archive & Distribution System (LAADS) Distributed Active Archive Center (DAAC; https://ladsweb.nascom.nasa.gov/). The MODIS IR PWV measurements (PWV_{IR}) are generated from the MYD05_L2 data at 5 km × 5 km pixel resolution (at nadir) during both day and night (Borbas and Menzel, 2015), when at least nine Field of Views (FOVs) are cloud-free. The MYD05_L2 and MYD03_L1 data are used to measure the clear-sky MODIS nIR retrievals (PWV_{nIR}) at 1 km × 1 km pixel resolution (at nadir) during daytime, which are further incorporated to assess the performance of PWV_{IR} under confident clear conditions over both ocean and land because the accuracy of PWV_{nIR} can be well-improved after linear regression adjustment (Li, 2004; Li et al., 2005). The cloud mask from MYD06_L2 data (Ackerman et al., 1998; Frey et al., 2008), derived from remotely sensed thermal infrared and solar reflected radiances, is used to identify the PWV_{nIR} under clear-sky conditions as well as to classify the PWV_{IR} into 4 groups, according to the clear-sky confidence level of each IR pixel. As a result, PWV_{IR} is divided into groups under > 99%, > 95%, > 66% and ≤ 66% probabilities of clear conditions, respectively.

Moreover, the European Centre for Medium-Range Weather Forecasts (ECMWF) Interim Reanalysis (ERA-Interim) (Dee et al., 2011) is a third generation of global atmospheric reanalysis from ECMWF, which uses a much-improved atmospheric model and assimilation system compared with those used in ERA-40. ERA-Interim represents a major undertaking by ECMWF, with several of the inaccuracies exhibited by ERA-40 being eliminated or significantly reduced. By using the rain-affected radiances from passive microwave imagers as observations, the PWV value was initially retrieved based on an off-line, one-dimensional variational (1D-Var) retrieval scheme, and it was then assimilated and reanalyzed in four-dimensional variational (4D-Var), as a pseudo-observation in ERA-Interim (Dee et al., 2011). In this study, total column water vapor from ERA-Interim reanalysis at 0.5° resolution, available every six hours (i.e., 00 h, 06 h, 12 h and 18 h UTC), is adopted as the a priori value of the CDLAM, during the MODIS IR water vapor product adjustment.

Furthermore, in order to evaluate the performance of PWV_{IR} under

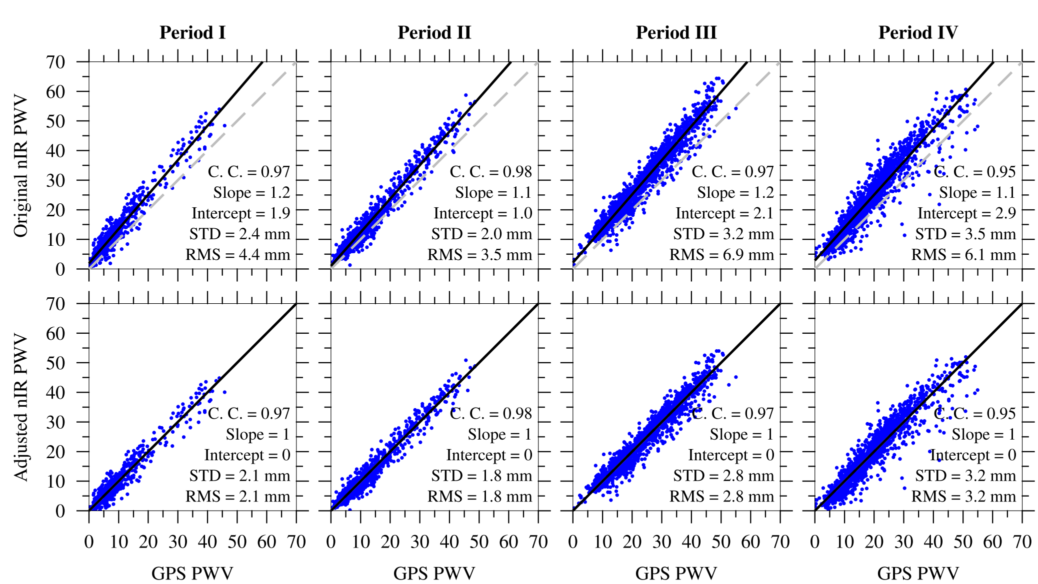

Fig. 5. Scatterplots of original (top row) and adjusted (bottom row) PWV_{nIR} under confident clear conditions against PWV_{GPS} during periods I, II, III and IV, respectively. Dashed gray lines: zero-bias lines. Solid black lines: linear regression results.

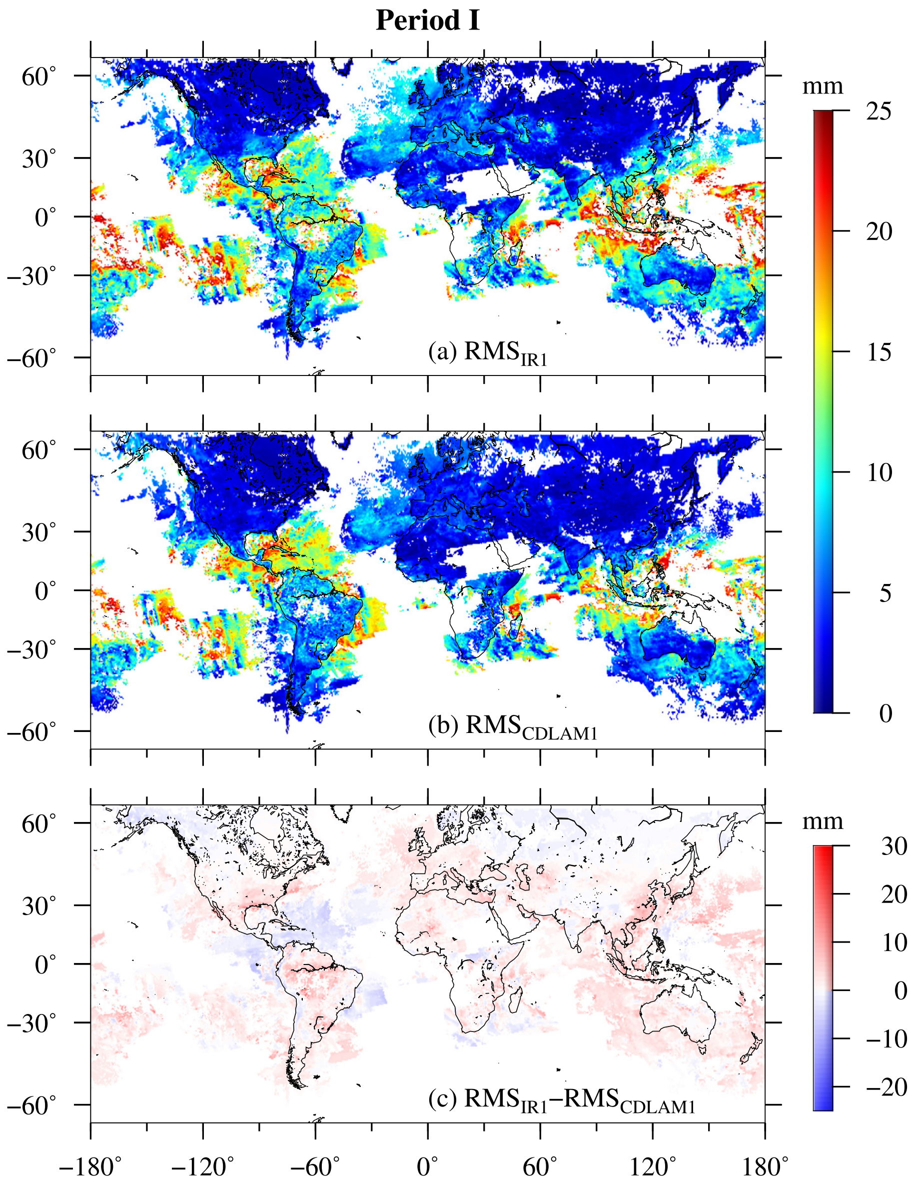

Fig. 6. The 0.5° gridded RMS distributions of (a) PWV_{IR} and (b) PWV_{CDLAM} against the adjusted PWV_{nIR} under confident clear conditions, as well as (c) their RMS difference between 65 °N and 65 °S, during time period I from 11 to 17 January 2015. Note that the white areas in (a) and (b) are affected by the exclusion of MODIS nIR images with no GPS data in the coverage, the presence of clouds, as well as not determined MODIS cloud mask flag (i.e., the value of bit 0 in the MODIS cloud mask scientific data set (SDS) equals to 0).

different probabilities of clear conditions, PWV measurements from ground-based GPS observations (PWV_{GPS}) are also incorporated in this study. When travelling from GPS satellites to ground based GPS receivers, the radio signals are delayed by the ionosphere and the neutral atmosphere. The ionosphere delay is frequency-dependent and can be removed up to 99% with the data from dual-frequency GPS receivers (Brunner and Gu, 1991). The zenith delay of the neutral atmosphere (i.e., zenith total delay (ZTD)) can be split into zenith hydrostatic delay (ZHD) caused by dry gases and zenith wet delay (ZWD) caused by the water vapor in the atmosphere. Using pressure observations (P_s; in mbar) measured directly at the surface, the ZHD can be estimated by (Elgered et al., 1991)

$$ZHD = (2.2779 \pm 0.0024)P_s/f(\phi, h) \tag{1}$$

$$f(\phi, h) = 100.00266\,cos(2\phi) - 0.00028h \tag{2}$$

where $f(\phi,h)$ accounts for the variation in gravitational acceleration with latitude ϕ and height h of the surface above the ellipsoid (in km). Once ZHD is calculated, ZWD is obtained by subtracting ZHD from ZTD, and it is converted into PWV by (Bevis et al., 1992)

$$PWV = \Pi \times ZWD \tag{3}$$

where Π is the empirical factor, which can be obtained by the water vapor weighted mean temperature T_m. T_m is computed from surface air temperature T_s at co-located GPS sites with the linear regression analysis (Bevis et al., 1992).

SuomiNet is a university organized real-time GPS network with surface meteorological observations, which provides easy access to a large and growing network to derive PWV_{GPS} measurements (Ware et al., 2000). PWV_{GPS} data product from SuomiNet used in this study is obtained from the University Corporation for Atmospheric Research (UCAR; https://www.suominet.ucar.edu/data.html). Nevertheless, considering that some GPS sites are not included in SuomiNet, especially outside the USA, we also estimated PWV_{GPS} from the GPS ZWD product and co-located surface meteorological observations with Eq. (3). Both the GPS ZWD product and surface meteorological

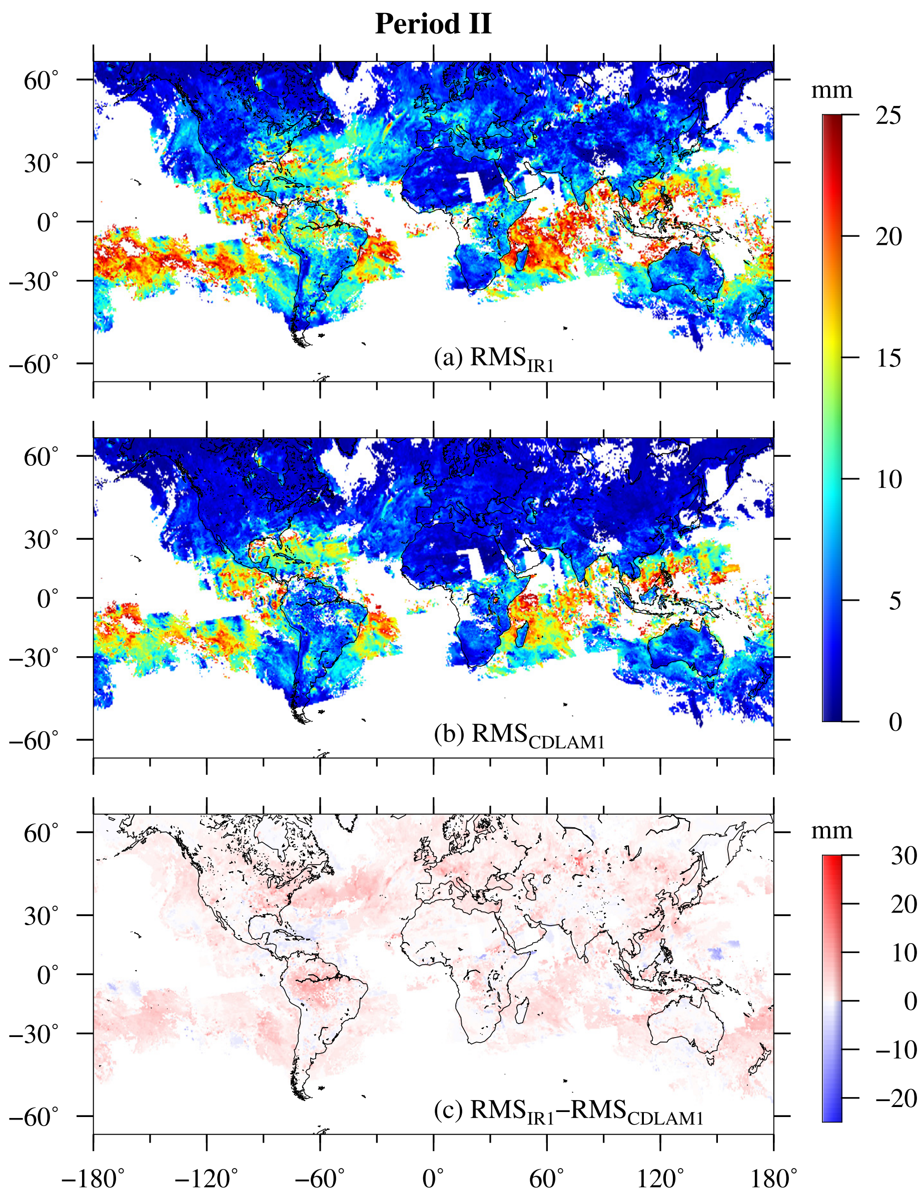

Fig. 7. Similar to Fig. 6, but during the time period II, from 11 to 17 April 2015.

observations are obtained from the Scripps Orbit and Permanent Array Centre (SOPAC, http://sopac.ucsd.edu/). The GPS ZWD product is estimated for each UTC day in the Jet Propulsion Laboratory (JPL) MEaSUREs processing, by adopting the PPP strategy, as implemented in the GIPSY-OASIS II software (Zumberge et al., 1997). PWV_{GPS} measurements from SuomiNet and SOPAC are then spatio-temporally synchronized with PWV_{nIR} and/or PWV_{IR}, using the nearest neighbor method for comparison. As a result, a total of 702 GPS sites between 65° S – 65° N are incorporated in this study.

2.2. Cloud mask related differential linear adjustment model

In order to integrate PWV_{IR} under different probabilities of clear conditions, we further develop a CDLAM for MODIS IR water vapor product in this study. The CDLAM can be performed as follows (see also Fig. 1).

1) Classify PWV_{IR} pixels into 4 groups according to the MYD06_L2 product. The groups denote PWV_{IR} values under > 99%, > 95%, > 66% and ≤ 66% probabilities of clear conditions.
2) Obtain the a priori PWV value (PWV_{ERA}) from ERA-Interim reanalysis at the MODIS overpass time and at MODIS pixel locations via spline and inverse distance weight (IDW) interpolations in temporal and spatial domains, respectively.
3) For the spatio-temporally synchronized PWV_{IR} and PWV_{ERA} data pairs in each group, remove the outliers that are more than three standard deviations (3σ) away from the mean, and obtain the differential PWV (ΔPWV) for each group by subtracting PWV_{ERA} from PWV_{IR}.
4) Assume that the linear relationship between ΔPWV and PWV_{IR} is defined by the equation $\Delta PWV = a \cdot PWV_{IR} + b$, where a is the slope, and b is the intercept. For each group, implement the linear least square (LS) regression analysis between ΔPWV and PWV_{IR} to derive the parameters a and b, and then get the fitting differential water vapor information by $\Delta PWV_f = a \cdot PWV_{IR} + b$.
5) Derive the PWV_{IR} adjustments (PWV_{CDLAM}) by subtracting ΔPWV_f from PWV_{IR} in each group.

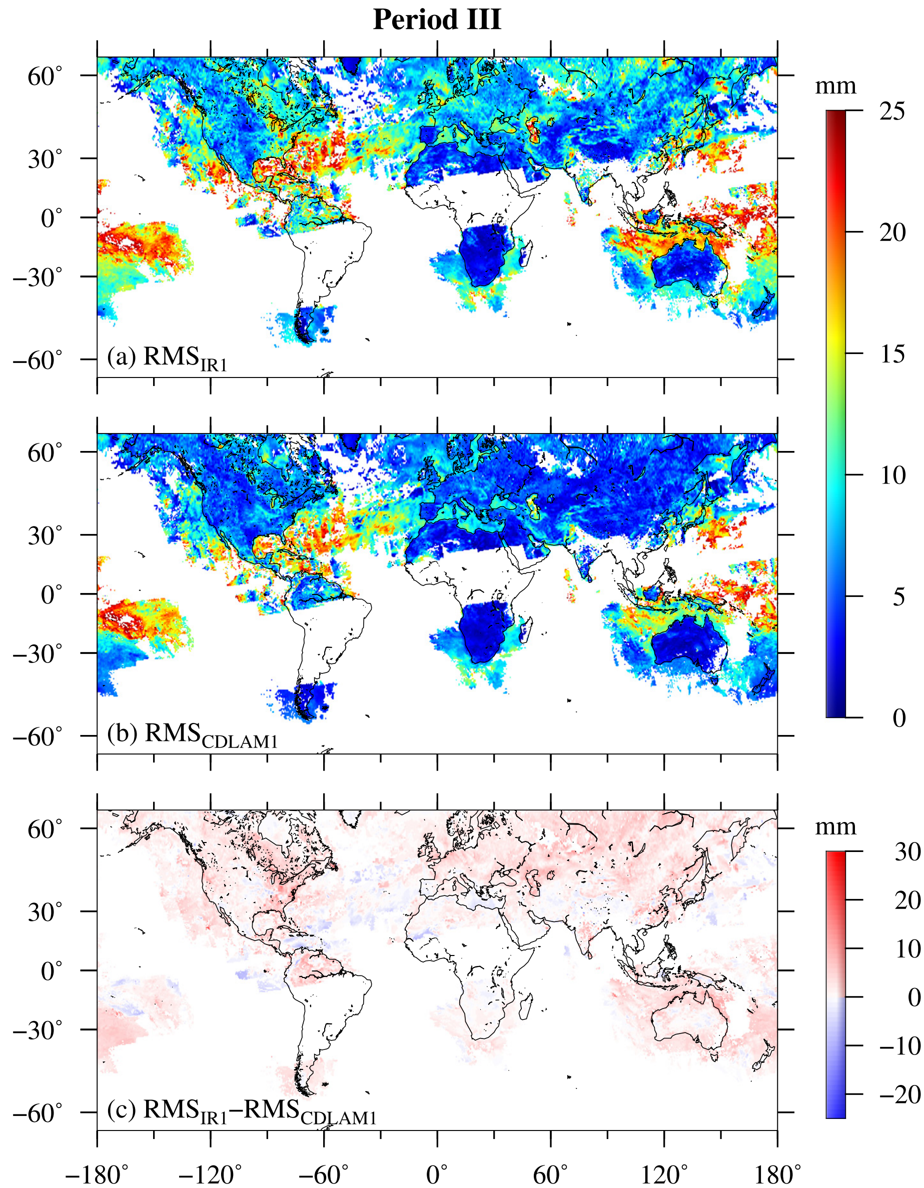

Fig. 8. Similar to Fig. 6, but during the time period III, from 10 to 16 July 2015.

3. MODIS IR PWV adjustment: Case studies in the USA

In this section, two MODIS images acquired during daytime at 19:50 UTC on 11 July 2015 (MOD1), and at 19: 50 UTC on 16 January 2015 (MOD2) in the USA are selected to test the performance of the CDLAM during PWV_{IR} adjustment. Apart from CDLAM, the traditional linear LS regression analysis between PWV_{ERA} and PWV_{IR} is also implemented to obtain the LS-adjusted IR retrievals (PWV_{LS}) for comparison. Note that data pairs with differences exceeding 3σ are excluded during the linear regression analysis in the LS model, which is similar to that in the CDLAM. The average PWV_{IR} in MOD1 and MOD2 is 32.4 mm and 11.0 mm, which provides us an opportunity to investigate the performance of the CDLAM under moist and dry atmospheres, respectively. Due to the availability of PWV_{nIR}, only daytime MODIS data are selected and PWV_{IR} under confident clear conditions are further evaluated with the adjusted PWV_{nIR}. Moreover, the MODIS images in the USA are selected since the high density of GPS sites is helpful to assess PWV_{IR} adjustments under different probabilities of clear conditions.

3.1. Comparison between PWV_{IR} and PWV_{nIR} under confident clear conditions

Before being used as the reference to evaluate PWV_{LS} and PWV_{CDLAM} adjustments in MOD1 and MOD2, PWV_{nIR} needs to be adjusted with the available GPS observations. Fig. 2 shows the scatterplots of the original and adjusted PWV_{nIR} under confident clear conditions against PWV_{GPS} in MOD1 and MOD2, respectively. It should be mentioned that despite a total of 138 and 160 GPS sites (Fig. 3) that are available in MOD1 and MOD2, PWV_{GPS} from only 43 and 50 GPS sites (see red triangles in Fig. 3) are used during the linear LS regression analysis between PWV_{nIR} and PWV_{GPS}, respectively. The exclusion of PWV_{GPS} during the PWV_{nIR} adjustment is due to the cloudiness of the spatio-temporally synchronized PWV_{nIR}.

As illustrated in Fig. 2, despite strong correlations between the original PWV_{nIR} and PWV_{GPS} found in both MOD1 and MOD2 (see Figs. 2(a) and 2(c)), obvious PWV discrepancies also exist in both cases. The standard deviation (STD) difference between the original PWV_{nIR} and PWV_{GPS} is 3.3 mm and 1.0 mm, and the root mean square (RMS) difference between them is 8.7 mm and 2.5 mm under moist and dry

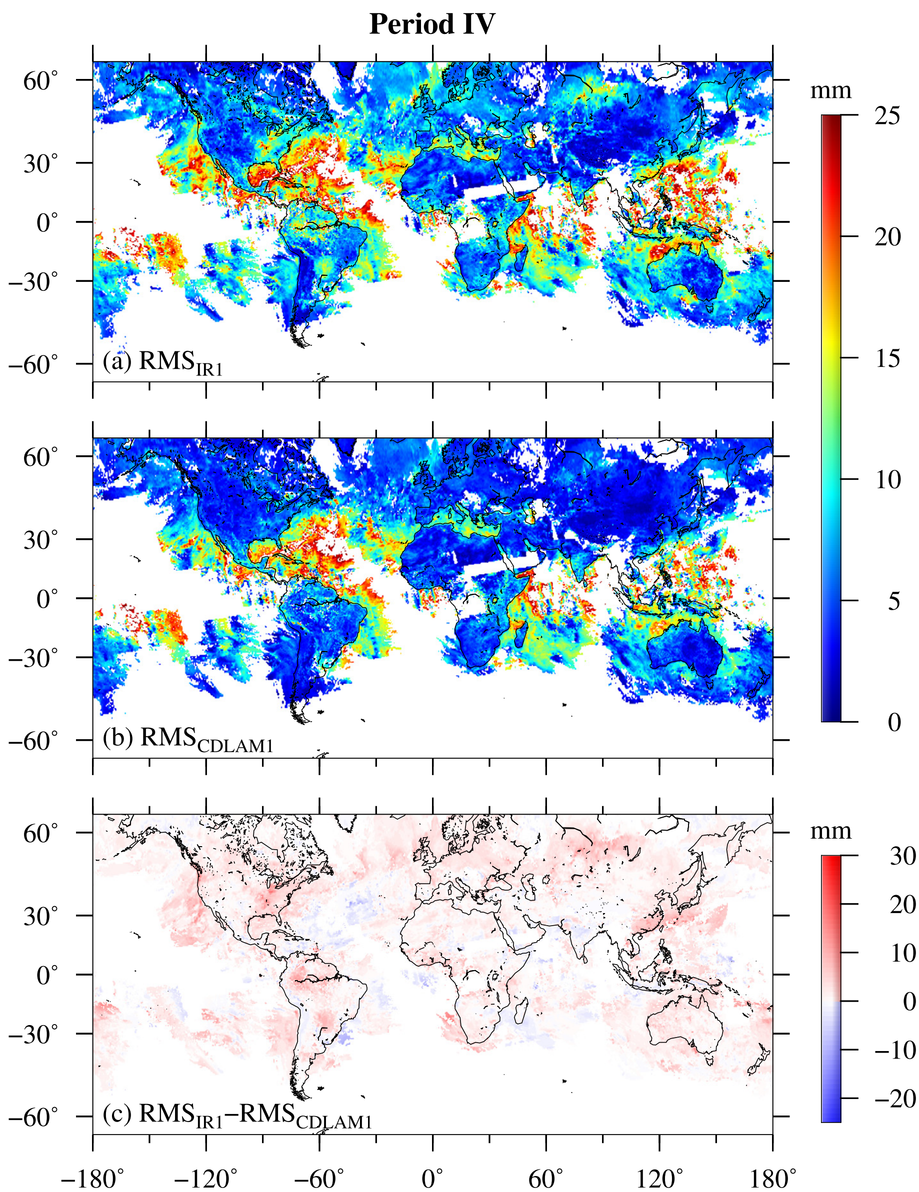

Fig. 9. Similar to Fig. 6, but during the time period IV, from 8 to 14 October 2015.

Table 2
The overall mean RMS difference of PWV$_{IR}$ and PWV$_{CDLAM}$ against the adjusted PWV$_{nIR}$ over ocean and land between 65° S~65° N under confident clear conditions during different time periods, respectively. (Unit: mm).

RMS	Location	Time periods			
		Period I	Period II	Period III	Period IV
RMS$_{IR1}$	Ocean	10.7	11.1	12.6	11.3
	Land	4.9	5.4	7.4	6.5
RMS$_{CDLAM1}$	Ocean	9.3	9.1	10.9	9.7
	Land	3.9	3.8	5.2	4.8

atmospheric conditions, respectively. The STD drops to 2.8 mm and 0.9 mm, together with the RMS, which is reduced to 2.7 mm and 0.8 mm after adjustment in MOD1 and MOD2, respectively. As a result, a STD improvement of 15% and 10% and a RMS improvement of 69% and 69% are achieved after the adjustments in MOD1 and MOD2, respectively, suggesting the reliabilities of the adjusted PWV$_{nIR}$ to further assess PWV$_{IR}$ before and after adjustment.

Fig. 3 shows the MODIS water vapor distributions from PWV$_{IR}$, PWV$_{LS}$, PWV$_{CDLAM}$ and the adjusted PWV$_{nIR}$ under confident clear conditions in MOD1 and MOD2, respectively. It is clear in Fig. 3 that PWV$_{IR}$ exhibits an obvious discrepancy compared with the adjusted PWV$_{nIR}$, and the overall mean RMS difference of PWV$_{IR}$ against the adjusted PWV$_{nIR}$ is 8.4 mm and 9.0 mm in MOD1 and MOD2, respectively. After adjusting with the LS model, the biases in PWV$_{IR}$ are further amplified in PWV$_{LS}$, and the overall mean RMS difference of PWV$_{LS}$ against the adjusted PWV$_{nIR}$ increases to 12.0 mm and 21.8 mm in MOD1 and MOD2, respectively. As such, the LS model may not be an appropriate choice to effectively improve PWV$_{IR}$. After adjusting with the CDLAM, the water vapor distribution from PWV$_{CDLAM}$ exhibits a similar pattern to that of the adjusted PWV$_{nIR}$. The overall mean RMS difference of PWV$_{CDLAM}$ against the adjusted PWV$_{nIR}$ is reduced to 6.3 and 3.2 mm in MOD1 and MOD2, indicating an improvement of 25% and 64% in PWV$_{CDLAM}$, under moist and dry atmospheric conditions, respectively.

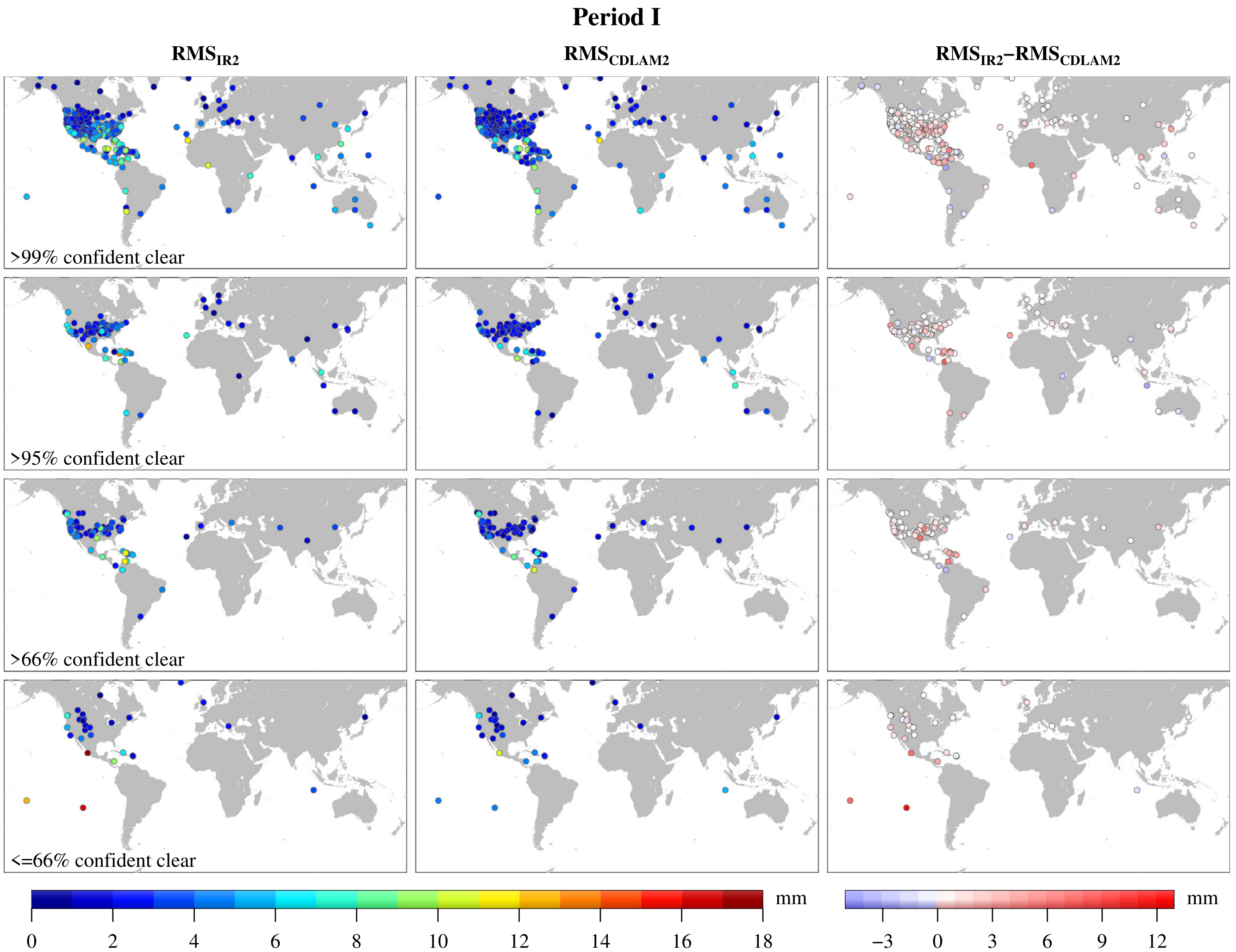

Fig. 10. RMS distributions of PWV_{IR} (left) and PWV_{CDLAM} (middle) against PWV_{GPS}, together with their RMS difference (right) during the time period I from 11 to 17 January 2015 under > 99% (top row), > 95% (second row), > 66%(third row) and ≤66% (bottom row) confident clear conditions.

3.2. Comparison between PWV_{IR} and PWV_{GPS} under different probabilities of clear conditions

In order to further assess the performance of PWV_{CDLAM} under different probabilities of clear conditions, comparisons of PWV values at available GPS sites among PWV_{IR}, PWV_{LS}, PWV_{CDLAM}, PWV_{ERA} and PWV_{GPS} at clear-sky confidence levels of > 99%, > 95%, > 66% and ≤ 66% in MOD1 and MOD2 are also made, respectively (see Fig. 4). Note that only 84 of 138 and 95 of 160 GPS sites (see the magenta triangles in Fig. 3) are compared in MOD1 and MOD2, respectively. The exclusion of the GPS sites is due to the presence of clouds, as well as the 3σ exclusion in the CDLAM. As can be seen in Fig. 4, although PWV_{ERA} is incorporated in both the CDLAM and the LS model, the performance of PWV_{CDLAM} and PWV_{LS} is remarkably different. While PWV_{CDLAM} gets closer to PWV_{GPS}, PWV_{LS} significantly deviates from PWV_{GPS} under all probabilities of clear conditions in both MOD1 and MOD2. Moreover, PWV_{ERA} uncertainties may not be the primary cause of the inferiority of the LS model to the CDLAM, since the RMS differences of the incorporated PWV_{ERA} against PWV_{GPS} are smaller than those of PWV_{IR} in both cases (Table 1).

Taking PWV_{GPS} as the reference, the RMS difference of PWV_{LS} is increased by 5.5 mm, 10.0 mm, 8.0 mm and 11 mm in MOD1, as well as by 8.0 mm, 19.5 mm, 23.4 and 8.4 mm in MOD2 under > 99%, > 95%, > 66% and ≤ 66% confidence of clear conditions (see also Table 1), respectively. On the contrary, after adjusting with the CDLAM, the RMS difference of PWV_{CDLAM} is improved by 52%, 17%, 4% and 52% in MOD1, as well as 50%, 72%, 66% and 71% in MOD2 under > 99%, > 95%, > 66% and ≤ 66% confident clear conditions, respectively. Moreover, it is interesting to note that the performances of PWV_{CDLAM} under unconfident clear conditions are superior to those of PWV_{IR} under confident clear conditions in both cases (Table 1), suggesting the possibility of exploiting the MODIS IR water vapor retrievals under all probabilities of clear conditions.

4. Global (65° S∼65° N) performance assessment of the CDLAM

Given that the atmospheric water vapor status in the USA is not representative of the global weather (Liou et al., 2001), we further investigate the global (65° S∼65° N) robustness of the CDLAM in this section. The performance evaluation of both PWV_{IR} and PWV_{CDLAM} over the polar regions is not implemented, owing to the low frequency of the MODIS confident clear conditions over the Arctic (Chan and Comiso, 2013) and the Antarctic (Bromwich et al., 2012). Four time periods of one-week MODIS IR water vapor retrievals in 2015, i.e., from 11 to 17 January (period I), from 11 to 17 April (period II), from 10 to 16 July (period III) and from 8 to 14 October (period IV), respectively, are adjusted with CDLAM. Considering that MODIS IR water vapor retrievals are available during both daytime and night time, we process all available 288 MODIS IR images on each day, giving 2016 images during each time period. PWV_{CDLAM} is then assessed via comparison

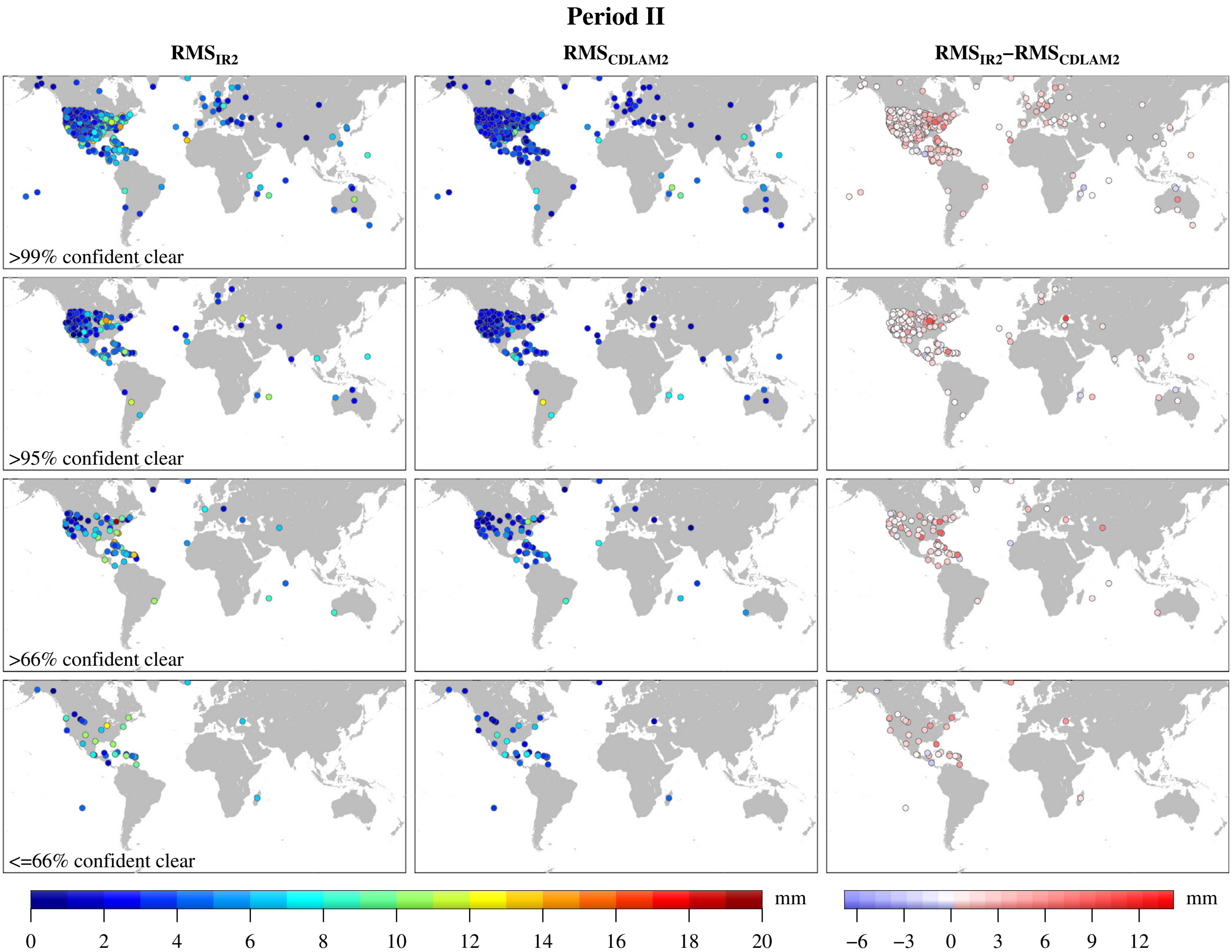

Fig. 11. Similar to Fig. 10, but during time period II, from 11 to 17 April 2015.

with the LS-adjusted PWV_{nIR} in the daytime under confident clear conditions over both land and ocean (Section 4.1), as well as PWV_{GPS} during both daytime and night time under different probabilities of clear conditions (Section 4.2), respectively.

4.1. Global evaluation of PWV_{CDLAM} using PWV_{nIR} under confident clear conditions

In Fig. 5, comparison of the original and the adjusted PWV_{nIR} under confident clear conditions against PWV_{GPS} during each time period are made. As we can see in Fig. 5, the correlation coefficients (CCs) between PWV_{nIR} and PWV_{GPS} are > 0.95 before and after adjustment during each time period. In addition, the RMS differences in periods III and IV are larger than those in periods I and II. The reason may be that most of the available GPS observations are located in the Northern Hemisphere (see Fig. 10 below), where the warmer atmosphere in July and October holds more moisture than in January and April. After implementing the LS adjustment, a STD improvement of 14%, 12%, 13% and 10%, as well as a RMS improvement of 53%, 49%, 60% and 49% is achieved in periods I, II, III and IV, respectively. It should be also mentioned that only MODIS nIR images with at least one GPS site available in the coverage are adjusted for further comparison during each time period, since the absence of GPS observations could lead to the biases in the adjusted PWV_{nIR}.

Taking the adjusted PWV_{nIR} as the reference, the RMS distribution of PWV_{IR} (RMS_{IR1}) and PWV_{CDLAM} (RMS_{CDLAM1}), as well as their difference (RMS_{IR1} minus RMS_{CDLAM1}) at 0.5° × 0.5° grids between 65°S–65°N under confident clear conditions, during periods I–IV, is shown in Figs. 6–9, respectively. As illustrated in Fig. 6(a), the larger values of RMS_{IR1} in January are generally observed more over the Southern Hemisphere than the Northern Hemisphere, which may be due to the fact that warmer air can hold more water vapor, and the uncertainties of PWV_{IR} are larger under warmer air. In addition, RMS_{IR1} values are also generally larger at tropical regions (−30°S–30°N) than at middle and high latitudes (−65°S–−30°S and 30°N–65°N), as well as larger over ocean than land. After adjusting with the CDLAM, the overall mean RMS of PWV_{IR} against adjusted PWV_{nIR} drops from 4.9 mm and 10.7 mm in RMS_{IR1} to 3.9 mm and 9.3 mm in RMS_{CDLAM1} over land and ocean (see also Table 2), respectively. PWV_{CDLAM} agree better with the adjusted PWV_{nIR} than PWV_{IR} over most land and ocean areas (see Fig. 6(b) and (c)), except over the oceanic areas at the low latitudes (e.g., northern South America). One of the most likely reasons for the inferiority of RMS_{CDLAM1} to RMS_{IR1} over the above mentioned oceanic areas may result from the absence of reference data (i.e., PWV_{GPS}) during PWV_{nIR} adjustment over the ocean from time to time as analyzed in Fig. 5. Furthermore, the uncertainties of the CDLAM itself could also lead to the discrepancy between PWV_{CDLAM} and the adjusted PWV_{nIR}.

RMS_{IR1} and RMS_{CDLAM1} during period II, shown in Fig. 7, exhibit similar results as in Fig. 6, except that RMS_{CDLAM1} is larger than RMS_{IR1} mainly over the oceanic areas between the equator and 30 °N (see Fig. 7(c)). After the implementation of the CDLAM, an overall mean

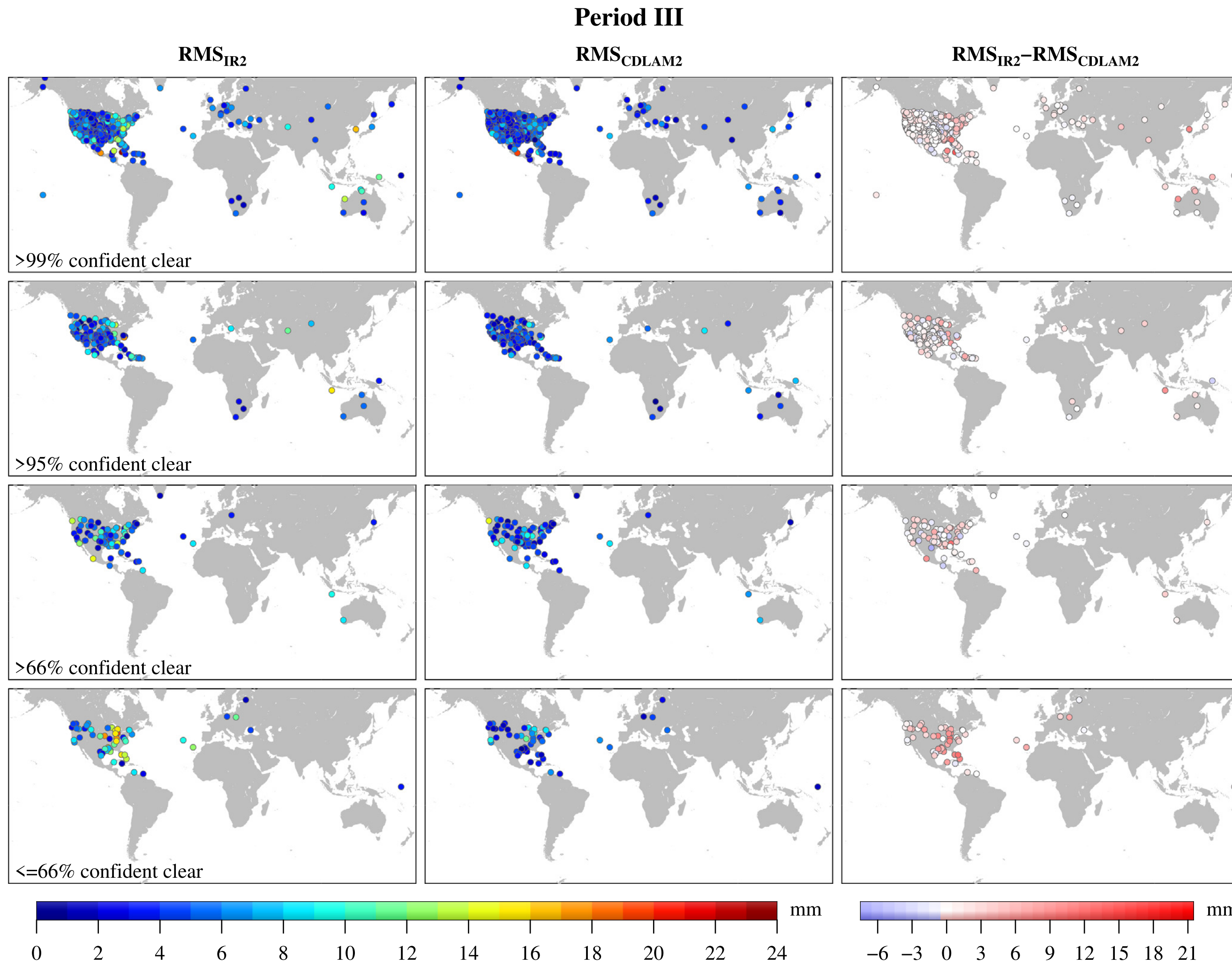

Fig. 12. Similar to Fig. 10, but during time period III, from 10 to 16 July 2015.

RMS improvement of 18.0% and 29.6% is achieved during period II over ocean and land (see also Table 2), respectively. In Figs. 8 and 9, RMS_{IR1} during periods III and IV are generally larger over the Northern Hemisphere than the Southern Hemisphere, which is opposite to the results during periods I and II in Figs. 6 and 7. Additionally, the inferiority of RMS_{CDLAM1} to RMS_{IR1} in periods III and IV is mainly over low-latitude oceans (see Figs. 8(c) and 9(c)), which is similar to the results during periods I and II. After adjusting with the CDLAM, the uncertainties in PWV_{IR} during periods III and IV are also mitigated, with an overall mean RMS improvement of 13.5% and 29.7% during period III, and 14.2% and 26.2% during period IV over ocean and land (see also Table 2), respectively.

4.2. Global evaluation of PWV_{CDLAM} using PWV_{GPS} under different probabilities of clear conditions

In order to further evaluate the performance of the CDLAM during both daytime and night time under different probabilities of clear conditions, comparisons of PWV_{IR} and PWV_{CDLAM} with PWV_{GPS} between 65°S–65°N are made in this subsection. The RMS distributions of PWV_{IR} (RMS_{IR2}) and PWV_{CDLAM} (RMS_{CDLAM2}) against PWV_{GPS}, as well as their differences (RMS_{IR2} minus RMS_{CDLAM2}) at available GPS sites under different confident clear conditions during periods I–IV, are shown in Figs. 10–13, respectively. As illustrated in Figs. 10–13, both RMS_{IR2} and RMS_{CDLAM2} are generally larger at tropical regions than at middle and high latitudes, under different probabilities of clear conditions during all time periods, which is consistent with the analysis in Section 4.1 when referring to the adjusted PWV_{nIR}. In addition, as we can see in Figs. 10–13 and Table 3, the overall RMS_{IR2} under > 66% and ≤66% confident clear conditions, are obviously larger than those under > 99% and > 95% confident clear conditions, during all time periods except period I, indicating PWV_{IR} under confident clear conditions of > 66% and ≤66% should be used with extreme caution.

As also shown in Figs. 10–13, the uncertainties in PWV_{IR} are generally reduced after adjusting with the CDLAM under different probabilities of clear conditions during all time periods. Moreover, the overall mean RMS_{CDLAM2} under unconfident clear conditions is significantly smaller than the overall mean RMS_{IR2} under confident clear conditions during all time periods (see Table 3). It is inspiring that the superiority of the unconfident PWV_{CDLAM} to the confident PWV_{IR} observed in Section 3.2 is further confirmed in the global assessment, indicating the exploitability of PWV_{IR} under unconfident clear conditions. As a result, an overall mean RMS improvement of 31%, 29%, 36% and 40% during period I; 38%, 35%, 40% and 36% during period II; 26%, 22%, 25% and 51% during period III; and 36%, 29%, 33% and 37% during period IV is achieved under > 99%, > 95%, > 66% and ≤66% confident clear conditions (Table 3), respectively. Accordingly, we can conclude that not only can the CDLAM be helpful to improve the accuracy of PWV_{IR} under both confident and unconfident clear conditions, but it also can be adopted to exploit the PWV_{IR} under unconfident clear conditions.

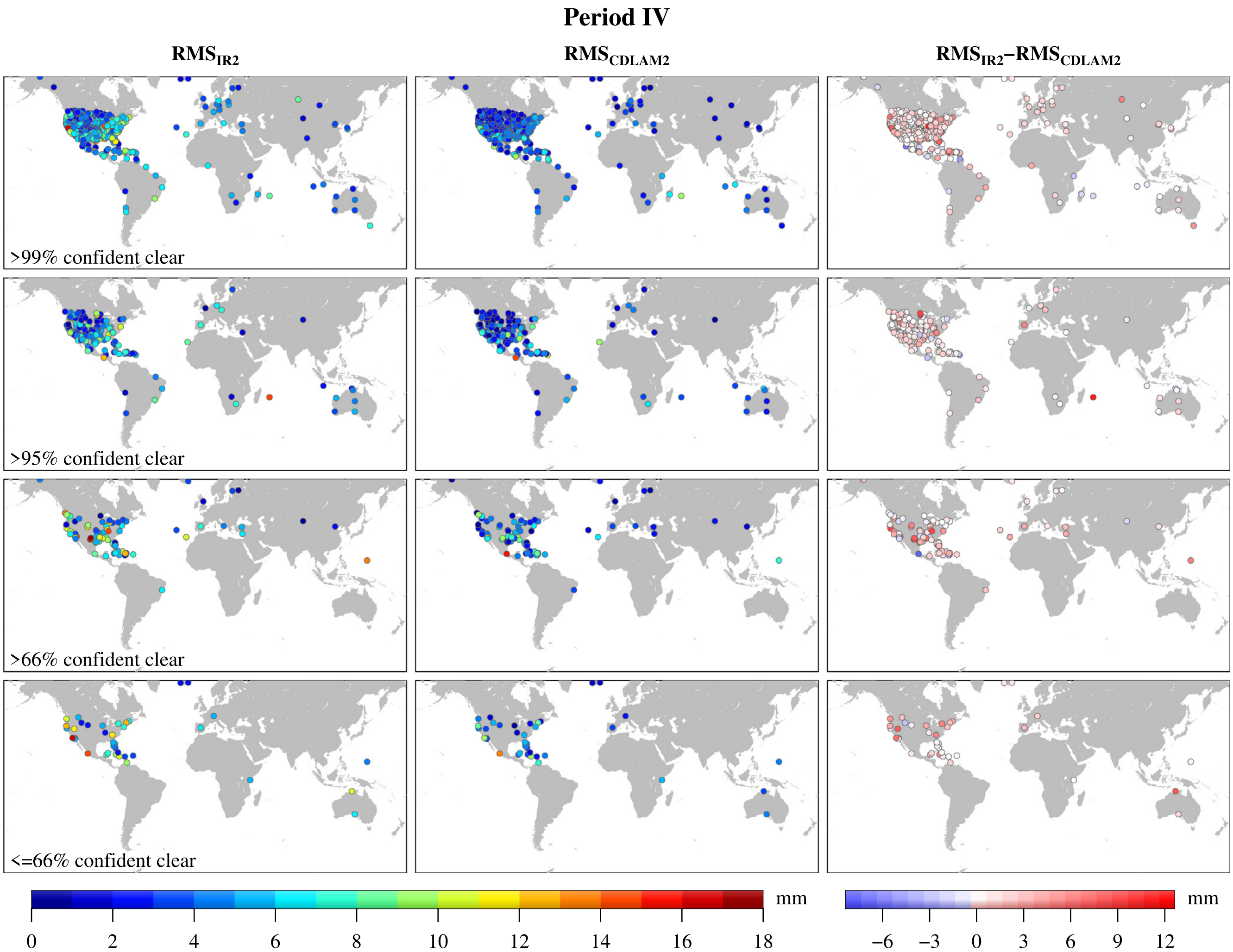

Fig. 13. Similar to Fig. 10, but during time period IV, from 8 to 14 October 2015.

Table 3
The overall mean RMS difference of PWV_{IR}, PWV_{CDLAM}, PWV_{LS} and PWV_{ERA} against PWV_{GPS} (designated as RMS_{IR2}, RMS_{CDLAM2}, RMS_{LS2}, and RMS_{ERA2}, respectively) at different clear-sky confidence levels during each time period. (Unit: mm).

Time periods	RMS	Clear-sky confidence levels			
		> 99%	> 95%	> 66%	≤66%
Period I	RMS_{IR2}	4.2	3.5	3.9	4.3
	RMS_{CDLAM2}	2.9	2.5	2.5	2.6
	RMS_{LS2}	8.5	9.6	10.3	11.4
	RMS_{ERA2}	2.4	2.2	2.4	2.1
Period II	RMS_{IR2}	4.8	4.0	5.5	6.4
	RMS_{CDLAM2}	3.0	2.6	3.3	4.1
	RMS_{LS2}	17.0	11.9	14.3	15.7
	RMS_{ERA2}	2.5	2.5	2.7	3.1
Period III	RMS_{IR2}	5.8	5.1	5.9	8.7
	RMS_{CDLAM2}	4.3	4.0	4.4	4.3
	RMS_{LS2}	11.7	12.5	14.6	27.5
	RMS_{ERA2}	3.8	3.7	3.9	3.7
Period IV	RMS_{IR2}	5.9	4.9	6.7	7.4
	RMS_{CDLAM2}	3.8	3.5	4.5	4.7
	RMS_{LS2}	14.2	10.6	14.8	386.5
	RMS_{ERA2}	4.7	3.3	3.7	3.3

5. Discussion

In this section, we further quantify the extent of the CDLAM to improve the availability of MODIS IR retrievals, as well as discuss the possible reasons for the improvement in the CDLAM. In Fig. 14, the daily mean percentage of the available PWV_{IR} and PWV_{CDLAM} grids in the MODIS IR image at different clear-sky confidence levels during all time periods is shown. As we can see in Fig. 14, the daily mean percentage of available PWV_{IR} grids under confident clear conditions is largest during each time periods, followed by the clear-sky confidence levels of > 95%, ≤66% and > 66%, respectively. The overall mean percentage of the available PWV_{IR} is 25.3%, 7.4%, 3.0% and 5.6% under > 99%, > 95%, ≤66% and > 66% confident clear conditions, respectively. After the implementation of the CDLAM, the overall mean percentage of the available MODIS IR retrievals is reduced slightly by 1.1%, 0.4%, 0.1% and 0.3% at clear-sky confidence levels of > 99%, > 95%, ≤66% and > 66%, respectively, due to the exclusion of outliers in the CDLAM. Nevertheless, after incorporating the CDLAM-adjusted IR retrievals under unconfident clear conditions, a data availability improvement of 14% is achieved during the selected time periods. Hence, the advantages of the CDLAM mainly lie in two aspects. On one hand, the CDLAM can significantly enhance the accuracy of PWV_{IR} under all probabilities of clear conditions. On the other hand, the performance of PWV_{CDLAM} under unconfident clear conditions is much better than that of PWV_{IR} under confident clear conditions. As such, the MODIS IR retrievals can be obtained with enhanced accuracy

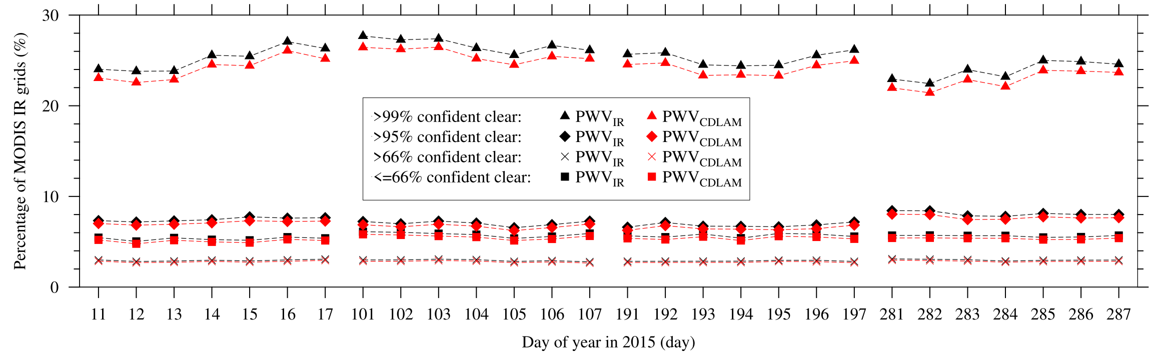

Fig. 14. Daily mean percentage of the available PWV_{IR} (black symbols) and PWV_{CDLAM} (red symbols) grids in the MODIS IR image under > 99% (triangles), > 95% (diamonds), > 66% (crosses) and ≤66% (squares) confidence of clear conditions during all time periods, respectively. (For interpretation of the references to colour in this figure legend, the reader is referred to the web version of this article.)

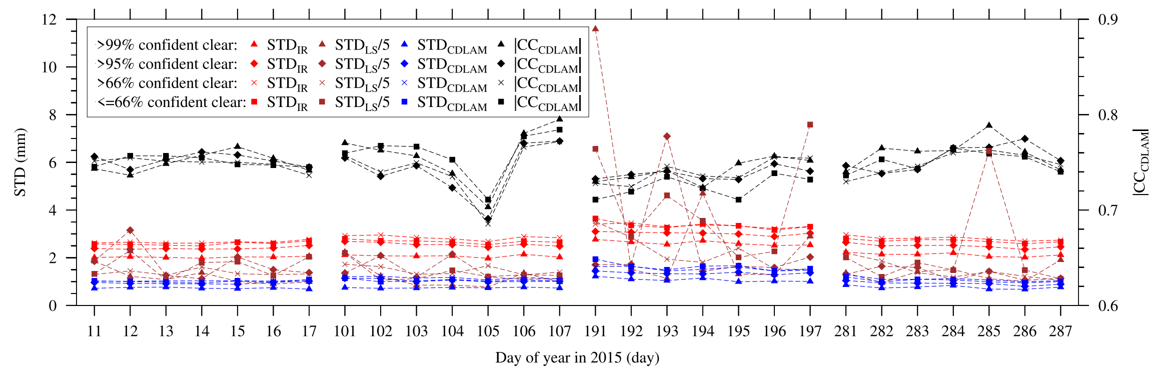

Fig. 15. Daily mean STD of PWV_{IR}, PWV_{LS} and ΔPWV_f against PWV_{ERA} (STD_{IR}, STD_{LS}, STD_{CDLAM}, respectively) and daily mean $|CC|$ of the linear regression analysis between PWV_{ERA} and ΔPWV_f ($|CC_{CDLAM}|$) at different clear-sky confidence levels during all time periods. Red, brown, blue and black symbols represent STD_{IR}, STD_{LS}, STD_{CDLAM} and $|CC_{CDLAM}|$, respectively, and triangles, diamonds, crosses and squares are the statistics under > 99%, > 95%, > 66% and ≤66% confident clear conditions, respectively. STD_{LS} shown in this figure denotes only 1/5th of the realistic result. (For interpretation of the references to colour in this figure legend, the reader is referred to the web version of this article.)

and improved data availability after adjusting with the CDLAM.

As described in Sections 2.2 and 3, the linear regression analysis is incorporated in both the CDLAM and the LS model. However, the linear regression analysis is performed between PWV_{ERA} and PWV_{IR} to derive PWV_{LS} directly in the former, whereas it is implemented twice for different purposes in the latter. The linear regression analysis between PWV_{ERA} and PWV_{IR} performed at the first time (step 3 in Section 2.2) is used to exclude the outliers in PWV_{IR} due to 3σ, which is the same as that in the LS model. In addition, the linear regression analysis between ΔPWV and PWV_{IR} performed at the second time (step 4 in section 2.2) is used to estimate the fitting differential water vapor information ΔPWV_f. Hence, the distinct difference between the CDLAM and the LS model lies in the fact that they implement the linear regression analysis in different ways. In order to investigate the potential causes for the accuracy enhancement in the CDLAM, we analyze the STD and the absolute value of CC ($|CC|$) of the linear regression analysis between PWV_{ERA} and PWV_{IR} (designated as STD_{IR} and $|CC_{IR}|$, respectively); those between PWV_{ERA} and PWV_{LS} (designated as STD_{LS} and $|CC_{LS}|$, respectively), as well as those between PWV_{ERA} and ΔPWV_f (designated as STD_{CDLAM} and $|CC_{CDLAM}|$, respectively) for each MODIS image. As a result, $|CC_{IR}|$, $|CC_{LS}|$ and $|CC_{CDLAM}|$ are the same as each other, STD_{LS} is found to be remarkably larger than STD_{IR}, and together with STD_{CDLAM} appears to be significantly smaller than STD_{IR} for each scene (not shown).

In Fig. 15, the daily mean STD_{IR}, STD_{LS}, STD_{CDLAM} and $|CC_{CDLAM}|$ under different confident clear conditions during all time periods are illustrated. Note that the daily mean $|CC_{LS}|$ and $|CC_{IR}|$ are not shown in Fig. 15 since they are always equal to the daily mean $|CC_{CDLAM}|$. In addition, STD_{LS} has been divided by 5 for better comparison. It is clear in Fig. 15 that the daily mean $|CC_{CDLAM}|$ under different confident clear conditions is > 0.68 during the linear regression analysis and indicates the CDLAM can maintain the good correlation of the linear regression analysis after the differential process. Moreover, while the daily mean STD_{LS} is on average 285%, 230%, 177% and 303% larger than the daily mean STD_{IR}, the daily mean STD_{CDLAM} is on average 63%, 60%, 59% and 59% smaller than the daily mean STD_{IR} under > 99%, > 95%, > 66% and ≤66% confident clear conditions, respectively. The inferiority of STD_{LS} to STD_{IR} suggests that the LS model gains an insignificant contribution from the a priori PWV_{ERA} by implementing the linear regression analysis directly, which could be one of the important causes for the unsuccessful PWV_{LS} adjustment. On the contrary, the greatly diminished STD_{CDLAM} indicates that the CDLAM obtains a significant profit from the a priori PWV_{ERA} via the differential process, which is more beneficial to developing a more robust linear regression model. It is also worth mentioning that the much greater uncertainties in PWV_{LS} than PWV_{ERA} observed in Fig. 4 are confirmed in all time periods (see Table 3), implying that the PWV_{ERA} uncertainties are not the primary cause of the ineffectiveness of the LS model. Therefore, the most likely reason for the effectiveness of the CDLAM and its superiority to the LS model may be that the differential process dramatically shrinks the deviation between the a priori PWV_{ERA} and the differential water vapor information after the linear regression analysis.

6. Conclusion

In this study, we have developed the CDLAM to adjust MODIS IR retrievals under all probabilities of clear conditions. Case studies in the USA (i.e., MOD1 and MOD2) and global (65°S–65°N) analysis are both

conducted to assess the performance of the CDLAM. Our findings from this study can be summarized as follows:

(1) Comparison of PWV_{IR}, PWV_{LS} and PWV_{CDLAM} against the adjusted PWV_{nIR} under confident clear conditions in MOD1 and MOD2 suggests that the LS model appears not to be an appropriate choice to improve PWV_{IR} under both moist and dry atmospheric conditions. In addition, comparison of PWV_{IR} and PWV_{CDLAM} against PWV_{GPS} further shows that a RMS improvement of 52%, 17%, 4% and 52% in the moist case, together with 50%, 72%, 66% and 71% in the dry case, has been achieved in PWV_{CDLAM} under > 99%, > 95%, > 66% and ≤66% probabilities of clear conditions, respectively.
(2) Global evaluation of PWV_{IR} and PWV_{CDLAM} against the adjusted PWV_{nIR} under confident clear conditions shows that RMS_{IR1} and RMS_{CDLAM1} are generally both larger at tropical regions than at middle and high latitudes, as well as larger over the ocean than land. In addition, RMS_{CDLAM1} is superior to RMS_{IR1} over most land and ocean areas, with an overall mean RMS improvement of 20.4%, 29.6%, 29.7% and 26.2% over land, as well as 13.1%, 18.0%, 13.5% and 14.2% over the ocean, during time periods I, II, III and IV, respectively.
(3) Taking the global available PWV_{GPS} as the reference, the uncertainties in PWV_{IR} under > 66% and ≤66% probabilities of clear conditions are generally larger than those under > 99% and > 95% probabilities of clear conditions, suggesting PWV_{IR} at lower confident clear levels should be used with extreme caution. Moreover, the uncertainties in PWV_{IR} under all confident clear conditions can be reduced at most GPS sites after adjusting with the CDLAM. Furthermore, the overall mean RMS_{CDLAM2} under unconfident clear conditions is smaller than RMS_{IR2} under confident clear conditions, revealing that PWV_{CDLAM} under unconfident clear conditions can also be adopted for further applications.
(4) The most likely reason for the effectiveness of the CDLAM may be that the deviation of the differential water vapor information, derived by the differential process, is significantly reduced after the linear regression analysis at all clear-sky confidence levels. As such, the CDLAM could be a promising tool to improve the accuracy of PWV_{IR} under all probabilities of clear conditions over both the ocean and land and could enhance the data availability of the MODIS IR water vapor product (e.g., 14% during the analyzed time periods in this study) and provides more details of the water vapor distribution and variation.

Acknowledgment

We are grateful to Prof. Menghua Wang, Prof. Ping Yang, Prof. Yuei-An Liou and the other two anonymous reviewers for their constructive suggestions and insightful criticisms that substantially improved the quality of our work. L. Chang appreciates the supports from Prof. Steven Sherwood (the University of New South Wales (UNSW)) and Prof. Matt King (the University of Tasmania (UTAS)) during his visit at UNSW in 2017 and at UTAS in 2018, respectively. The authors would also like to thank the Level-1 and Atmosphere Archive & Distribution System (LAADS) Distributed Active Archive Center, the European Centre for Medium-Range Weather Forecasts (ECMWF), the University Corporation for Atmospheric Research (UCAR) and the Scripps Orbit and Permanent Array Centre (SOPAC) for providing their data. This work was supported by the Global Change Research Program of China [grant number 2015CB953900] and the National Natural Science Foundation of China [grant numbers 41506211, 41804005 and 41706210].

References

Ackerman, S.A., Strabala, K.I., Menzel, W.P., Frey, R.A., Moeller, C.C., Gumley, L.E., 1998. Discriminating clear sky from clouds with MODIS. J. Geophys. Res.-Atmos. 103, 32141–32157.
Bevis, M., Businger, S., Herring, T.A., Rocken, C., Anthes, R.A., Ware, R.H., 1992. GPS meteorology: remote sensing of atmospheric water vapour using the global positioning system. J. Geophys. Res. 97 (D14), 15787–15801.
Bevis, M., Businger, S., Chiswell, S., Herring, T.A., Anthes, R.A., Rocken, C., Ware, R.H., 1994. GPS meteorology - mapping zenith wet delays onto precipitable water. J. Appl. Meteorol. 33, 379–386.
Borbas, E., Menzel, W.P., 2015. MODIS atmosphere L2 water vapor product. In: NASA MODIS Adaptive Processing System. Goddard Space Flight Center, USA. https://doi.org/10.5067/MODIS/MYD05_L2.006.
Bromwich, D.H., Nicolas, J.P., Hines, K.M., Kay, J.E., Key, E.L., Lazzara, M.A., Lubin, D., McFarquhar, G.M., Gorodetskaya, I.V., Grosvenor, D.P., Lachlan-Cope, T., van Lipzig, N.P.M., 2012. Tropospheric clouds in Antarctica. Rev. Geophys. 50 (RG1004-1–RG1004-40).
Brunner, F.K., Gu, M., 1991. An improved model for dual frequency ionospheric correction of GPS observations. Manuscr. Geodaet. 16, 205–214.
Chahine, M.T., 1992. The hydrological cycle and its influence on climate. Nature 359, 373–380.
Chan, M.A., Comiso, J.C., 2013. Arctic cloud characteristics as derived from MODIS, CALIPSO, and CloudSat. J. Clim. 26, 3285–3306.
Chang, L., Gao, G.P., Jin, S.G., He, X.F., Xiao, R.Y., Guo, L.X., 2015. Calibration and evaluation of precipitable water vapor from MODIS infrared observations at night. IEEE Trans. Geosci. Remote Sens. 53, 2612–2620.
Dee, D.P., Uppala, S.M., Simmons, A.J., Berrisford, P., Poli, P., Kobayashi, S., Andrae, U., Balmaseda, M.A., Balsamo, G., Bauer, P., Bechtold, P., Beljaars, A.C.M., van de Berg, L., Bidlot, J., Bormann, N., Delsol, C., Dragani, R., Fuentes, M., Geer, A.J., Haimberger, L., Healy, S.B., Hersbach, H., Holm, E.V., Isaksen, L., Kallberg, P., Kohler, M., Matricardi, M., McNally, A.P., Monge-Sanz, B.M., Morcrette, J.J., Park, B.K., Peubey, C., de Rosnay, P., Tavolato, C., Thepaut, J.N., Vitart, F., 2011. The ERA-interim reanalysis: configuration and performance of the data assimilation system. Q. J. R. Meteorol. Soc. 137, 553–597.
Elgered, G., Davis, J.L., Herring, T.A., Shapiro, I.I., 1991. Geodesy by radio interferometry: water vapor radiometry for estimation of the wet delay. J. Geophys. Res. 96, 6541–6555.
Fan, S.J., Zang, J.F., Peng, X.Y., Wu, S.Q., Liu, Y.X., Zhang, K.F., 2016. Validation of atmospheric water vapor derived from ship-borne GPS measurements in the Chinese Bohai Sea. Terr. Atmos. Ocean. Sci. 27, 213–220.
Frey, R.A., Ackerman, S.A., Liu, Y.H., Strabala, K.I., Zhang, H., Key, J.R., Wang, X.G., 2008. Cloud detection with MODIS. Part I: improvements in the MODIS cloud mask for collection 5. J. Atmos. Ocean. Technol. 25, 1057–1072.
Held, I.M., Soden, B.J., 2000. Water vapor feedback and global warming. Annu. Rev. Energy Environ. 25, 441–475.
Kaufman, Y.J., Gao, B.C., 1992. Remote-sensing of water-vapor in the near IR from Eos/Modis. IEEE Trans. Geosci. Remote Sens. 30, 871–884.
King, M.D., Kaufman, Y.J., Menzel, W.P., Tanre, D., 1992. Remote-sensing of cloud, aerosol, and water-vapor properties from the moderate resolution imaging spectrometer (MODIS). IEEE Trans. Geosci. Remote Sens. 30, 2–27.
Li, Z., 2004. In: Production of Regional 1 km × 1 km water vapor fields through the integration of GPS and MODIS data. Proceedings of the 17th International Technical Meeting of the Satellite Division of the Institute of Navigation (ION GNSS 2004), Long Beach, California, USA, 21–24 Sep 2004. pp. 2396–2403.
Li, J., Wolf, W.W., Menzel, W.P., Zhang, W.J., Huang, H.L., Achtor, T.H., 2000. Global soundings of the atmosphere from ATOVS measurements: the algorithm and validation. J. Appl. Meteorol. 39, 1248–1268.
Li, Z.H., Muller, J.P., Cross, P., 2003. Comparison of precipitable water vapor derived from radiosonde, GPS, and moderate-resolution imaging Spectroradiometer measurements. J. Geophys. Res.-Atmos. 108.
Li, Z.H., Muller, J.P., Cross, P., Fielding, E.J., 2005. Interferometric synthetic aperture radar (InSAR) atmospheric correction: GPS, moderate resolution imaging spectroradiometer (MODIS), and InSAR integration. J. Geophys. Res. Solid Earth 110.
Li, Z.H., Fielding, E.J., Cross, P., Muller, J.P., 2006. Interferometric synthetic aperture radar atmospheric correction: medium resolution imaging spectrometer and advanced synthetic aperture radar integration. Geophys. Res. Lett. 33.
Li, Z.H., Pasquali, P., Cantone, A., Singleton, A., Funning, G., Forrest, D., 2012. MERIS atmospheric water vapor correction model for wide swath interferometric synthetic aperture radar. IEEE Geosci. Remote Sens. Lett. 9, 257–261.
Liou, Y.A., Teng, Y.T., Van Hove, T., Liljegren, J.C., 2001. Comparison of precipitable water observations in the near tropics by GPS, microwave radiometer, and radiosondes. J. Appl. Meteorol. 40, 5–15.
Liu, H.L., Tang, S.H., Zhang, S.L., Hu, J.Y., 2015. Evaluation of MODIS water vapour products over China using radiosonde data. Int. J. Remote Sens. 36, 680–690.
McCarthy, M.P., Thorne, P.W., Titchner, H.A., 2009. An analysis of tropospheric humidity trends from radiosondes. J. Clim. 22, 5820–5838.
Menzel, W.P., Schmit, T.J., Zhang, P., Li, J., 2018. Satellite-based atmospheric infrared sounder development and applications. Bull. Am. Meteorol. Soc. 99, 583–603.
Ross, R.J., Elliott, W.P., 2001. Radiosonde-based northern hemisphere tropospheric water vapor trends. J. Clim. 14, 1602–1612.
Schmit, T.J., Gunshor, M.M., Menzel, W.P., Gurka, J.J., Li, J., Bachmeier, A.S., 2005. Introducing the next-generation advanced baseline imager on goes-R. Bull. Am. Meteorol. Soc. 86, 1079.
Seemann, S.W., Li, J., Menzel, W.P., Gumley, L.E., 2003. Operational retrieval of atmospheric temperature, moisture, and ozone from MODIS infrared radiances. J. Appl. Meteorol. 42, 1072–1091.
Smith, W.L., Woolf, H.M., Hayden, C.M., Wark, D.Q., McMillin, L.M., 1979. The TIROS-N operational vertical sounder. Bull. Am. Meteorol. Soc., vol. 60, 1177–1187.

Steinke, S., Eikenberg, S., Lohnert, U., Dick, G., Klocke, D., Di Girolamo, P., Crewell, S., 2015. Assessment of small-scale integrated water vapour variability during HOPE. Atmos. Chem. Phys. 15, 2675–2692.

Ware, R.H., Fulker, D.W., Stein, S.A., Anderson, D.N., Avery, S.K., Clark, R.D., Droegemeier, K.K., Kuettner, J.P., Minster, J.B., Sorooshian, S., 2000. SuomiNet: a real-time national GPS network for atmospheric research and education. Bull. Am. Meteorol. Soc. 81, 677–694.

Wentz, F.J., Ricciardulli, L., Hilburn, K., Mears, C., 2007. How much more rain will global warming bring? Science 317, 233–235.

Yu, C., Li, Z.H., Penna, N.T., 2018. Interferometric synthetic aperture radar atmospheric correction using a GPS-based iterative tropospheric decomposition model. Remote Sens. Environ. 204, 109–121.

Zumberge, J.F., Heflin, M.B., Jefferson, D.C., Watkins, M.M., Webb, F.H., 1997. Precise point positioning for the efficient and robust analysis of GPS data from large networks. J. Geophys. Res. Solid Earth 102, 5005–5017.